JOURNAL OF SYNCHROTRON RADIATION
ISSN 1600-5775

Doping site identification in 112 iron pnictides through a first-principles core-electron spectroscopic study

Haranath Ghosh,[a,b]*‡ Soumyadeep Ghosh[a,b]‡ and Abyay Ghosh[a,b]

[a]Human Resources Development Section, Raja Ramanna Centre for Advanced Technology, Indore 452013, India, and [b]Homi Bhabha National Institute, Anushakti Nagar, Mumbai 400094, India.
*Correspondence e-mail: hng@rrcat.gov.in

Received 11 March 2019
Accepted 27 April 2019

Edited by I. Lindau, SLAC/Stanford University, USA

‡ These authors contributed equally to this work.

Keywords: Fe-based 112 superconducting materials; core-electron spectroscopy; core-hole effect; electronic structure calculations.

Density functional theory based first-principles core-electron spectroscopic studies on iron-based superconducting 112 materials are presented. The existence of an extra As zigzag chain structure along with Fe–As planes in 112 materials is emphasised. Doping on an As site belonging to a chain by Sb is found to enhance the superconducting transition temperature. This is also shown from calculations with enhanced density of states when doped on chain-As. Therefore, As site identification in 112 is crucial. Theoretically computed As *K*-edge absorption spectra of two different types of As atoms for $Ca_{0.85}La_{0.15}FeAs_2$ show a distinctly different nature. The sensitivities of As *K*-edge absorption spectra in the presence and absence of the 'core-hole effect' are presented for future possible identification of the same experimentally. In both cases absorption spectra contain several features, the origins of which are thoroughly described in terms of site projected density of states results.

1. Introduction

Core-electron spectroscopic techniques like X-ray absorption near-edge structure (XANES), electron energy-loss near-edge structure (ELNES), extended X-ray absorption fine structure (EXAFS) and their variants have endless applications in modern materials as well as various branches of science. These include energy materials (Singh *et al.*, 2018; Guo *et al.*, 2005), nuclear materials (Kosog *et al.*, 2012), medical science (Sarangi, 2018) and superconductors (Mizuguchi *et al.*, 2017) to mention a few. In core-electron spectroscopy, when the incident X-ray photon has an energy equal to or greater than the binding energy of a core-level electron (K = 1s; L_I = 2s; L_{II}/L_{III} = $2p_{1/2}/2p_{3/2}$ *etc.*), the X-ray photon is absorbed leading to ejection of the core-electron. This creates an excited state with an empty electronic level (core-hole) and the ejected photoelectron which carries excess energy being transited to the unoccupied conduction states, causing a sharp increase in absorption at a specific photon energy known as the absorption edge. X-ray absorption fine structure (XAFS) carries the fingerprint of the modulation of an atom's photon absorption coefficient at energies near and above the absorption edge due to its physical and chemical state. XAFS and X-ray absorption spectroscopy (XAS) have two absorption regions, XANES and EXAFS, depending on the energy dependence of absorption coefficient near and above the absorption edge. These two types of fine-structure features provide a wealth of information about an element's local structural environment and electronic state. For example, XAFS/XANES features that have a complicated origin carry

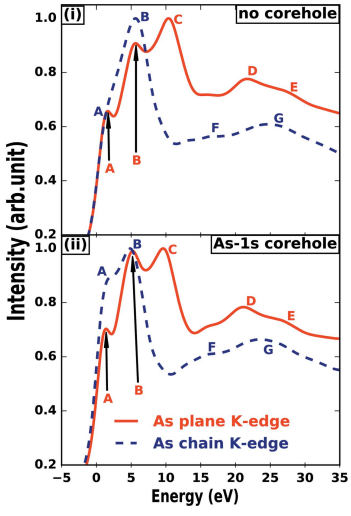

information about: (i) the local atomic probe (short-range order), (ii) the composition/coordination and (iii) the chemical/oxidation state; all the above apply to any element or phase (gas, liquid, crystalline, amorphous, *etc*.). XANES may consist of three subregions, namely 'pre-edge', 'edge' and 'near-edge', that are extremely sensitive to the chemistry of the absorbing atom, *e.g.* formal oxidation state, coordination environment and especially to the angular momentum of the unoccupied electronic states. A complete understanding of the physical/chemical processes and their computation, interpretation as well as application are subjects of current active research.

These specialties of the core-electron spectroscopic techniques mentioned above are traditionally used in various branches of condensed matter physics, including strongly correlated high-critical-temperature (T_c) superconductors (Bianconi *et al.*, 2017; Ivanov *et al.*, 2018) and recently discovered Fe-based high-temperature superconductors (Paris *et al.*, 2016). High-temperature superconductivity in Fe-based superconductors (IBSCs), discovered in 2008 (Kamihara *et al.*, 2008), remains as one of the greatest mysteries, *e.g.* 'Fe', usually known as a ferromagnetic element, plays a dominant role in high-T_c superconductivity. There exists a large number of families of Fe-based superconductors, all of them having the basic common feature of Fe-pnictogen/Fe-chalcogen layers. Apart from Fe-pnictogen (As) layers there exists an As zigzag chain between the Fe–As layers in one of the recently discovered IBSCs, namely the 112-family, discovered in 2013 with a superconducting T_c of 34 K (Katayama *et al.*, 2013). The blocking layers between the Fe–As layers are composed of Ca(La) spacer atoms as well as an As zigzag chain and, unlike other IBSCs, the Ca–As blocking layer is metallic and couples strongly with the FeAs layers (Wu *et al.*, 2014). A two-dimensional spin resonance mode at around $E \simeq 11$ meV was confirmed through inelastic neutron scattering measurements, where the resonance energy was found to be almost temperature independent and linearly scales with T_c signifying the possibility of sign-reversed ($s^{\pm}$) quasiparticle excitations between different Fermi surfaces in these multiband systems (Xie *et al.*, 2018). This was supported by theoretical electronic structure calculations which suggested that the energy and momentum distribution of the spin resonance does not directly respond to the k_z dependence of the fermiology (Xie *et al.*, 2018). More recently a systematic detailed electronic structure calculation of 112 materials has been presented (Ghosh *et al.*, 2019; Liu *et al.*, 2015; Huang *et al.*, 2015; Caglieris *et al.*, 2016). 112 materials are thought to be candidates for realizing topological superconductivity (Liu *et al.*, 2016). One of the important findings from the above studies is that a Lifshitz-like topological transition is shown to accompany orbital selective bandwidth modifications (Ghosh & Ghosh, 2019). Furthermore, one of the significant aspects is that the superconducting T_c can be raised up to 47 K, the highest value achievable in the 112 family, by Sb doping at the 'chain' As-site (Nagai *et al.*, 2015). Density functional theory (DFT) based studies predicted that Sb doping at the As-chain is more favourable than doping at the FeAs layer (Kudo *et al.*, 2014), which also subsequently received a favourable response from experimental studies (Ota *et al.*, 2017). Thus, As doping site identification (chain or plane) is extremely important as far as raising the T_c is concerned. This may also apply to other Fe-based superconductors having As-chain structure apart from plane (Kudo *et al.*, 2013). We argue and show that this can be achieved through site-element-specific XANES/ELNES studies. 112 materials have monoclinic crystal structure (space group $P2_1$, $P2_{1/m}$) with a zigzag chain of monovalent As atoms between alternate Ca–As space layers and trivalent As atoms in Fe–As plane layers. The presence of an arsenic zigzag chain is one of the most notable features in this family of IBSCs. This difference in As oxidation state of As atoms as well as its local environment in chain/plane gives rise to different absorption edges as well as different XANES/ELNES spectra. We note that no experimental or theoretical studies on XANES studies of 112 is available so far and thus we present the same for the As *K*-edge of $Ca_{0.85}La_{0.15}FeAs_2$ from plane and chain separately using first principles. Our results distinctly show the sensitivity of absorption edges depending on whether the As atom belongs to chain or plane. These results thus are likely to provide a useful guide to future experimental studies.

2. Theory and computational methodology

Essentially, the ELNES/XANES is nothing but the density of states (DOS) following modifications due to matrix elements between the correct initial and final states, a full discussion of which has been given by Egerton (1996). The physical background behind the calculation of ELNES in DFT-based numerical code *CASTEP* was reported earlier (Gao *et al.*, 2004, 2008, 2009; Pickard *et al.*, 1995; Pickard & Payne, 1997; Clark *et al.*, 2005; Jayawardane *et al.*, 2001; Sinha *et al.*, 2018) following several important steps. Firstly, for a *K*-edge, the dipole selection rule implies *p*-orbital partial DOS must be considered. The second relevant step is the accurate calculation of transition matrix elements between the initial and final states within the dipole approximation. The dipole approximation would apply to ELNES, for most transmission electron energy-loss spectroscopy experiments, especially when a small axial collection aperture is used. For XANES, a similar argument holds when the used incident wavelength of the X-ray is much larger compared with the size of the core orbital, the 1*s* core, in our case for the As *K*-edge. The (1*s*) core state ϕ_{1s}, being extremely localized, can be obtained from an all-electron atomic calculation. Calculation of unoccupied final state $\Psi_{n,k}$ involves the projector augmented wave (PAW) approach; an all-electron wavefunction can be recovered from the corresponding pseudo-wavefunction via a linear transformation (Blöchl, 1994) and matrix elements are suitably modified by some factor of projection operator (see below) for a given transition between an initial and final state. This approach also separates the plane wave model DOS into partial DOS results for each class of orbitals, for example *p* or *d etc*. While the initial state wavefunction can be calculated from an all-electron approach, based on atomic-like states, the

'excited' final state is ansatzed as a pseudo wavefunction in the PAW approach (Gao *et al.*, 2008),

$$\langle \phi_{1s}|r_\alpha|\Psi_{n,k}\rangle = \langle \phi_{1s}|r_\alpha|\tilde{\Psi}_{n,k}\rangle + \sum_i \left(\langle \phi_{1s}|r_\alpha|\phi_i\rangle - \langle \phi_{1s}|r_\alpha|\tilde{\phi}_i\rangle\right)\langle \tilde{p}_i|\tilde{\Psi}_{n,k}\rangle, \quad (1)$$

where ϕ_i and $\tilde{\phi}_i$ are all-electron and pseudopartial waves, respectively, and $\alpha = x, y, z$. $(\langle \phi_{1s}|r_\alpha|\phi_i\rangle - \langle \phi_{1s}|r_\alpha|\tilde{\phi}_i\rangle)$ can be evaluated once in real space for each pseudopotential used. $\tilde{p}_i$ is the PAW projector function, that we described above as the 'projection' factor, localized within the augmentation region, and obeys the relation $\langle \tilde{p}_i|\tilde{\phi}_i\rangle = 1$.

The intensity of ELNES spectra under the electric dipole approximation for transition from core states ϕ_{1s} to the group of final states $\psi_{n,k}$ is given as (Gao *et al.*, 2004, 2009)

$$I(E) = \sum_k \omega_k \left|\langle \Psi_{n,k}|\mathbf{r}_\alpha|\phi_{1s}\rangle\right|^2 \delta\left(E - E_{n,k}\right), \quad (2)$$

where E is measured with respect to the core level energy E_c, and the energy-conserving δ-function is replaced by Lorentzian function $\gamma(E - E_{n,k})$. One needs to generate a core-excited pseudopotential for one of the atoms where the core-hole is localized. However, the geometry for the core-excited sample is not relaxed, since the ionic relaxation time is expected to be larger than the electronic excitation. Thus, while the ionic and cell coordinates are updated with relaxed geometry for the non-excited atom, the test atom is replaced with a core-excited pseudopotential.

DFT-based first-principles calculations of ELNES and partial density of states (PDOS) are performed using the *Cambridge Serial Total Energy Package* (*CASTEP*) within the generalized gradient approximation (GGA) using the Perdew–Burke–Enzerhof (PBE) functional (Perdew *et al.*, 1996). The Broyden–Fletcher–Goldfrab–Shanno (BFGS) geometry optimization scheme has been used (Broyden, 1970; Fletcher, 1970; Goldfarb, 1970; Shanno, 1970). All atoms were fully relaxed until the magnitude of the force on each atom converged to less than 0.01 eV Å^{-1} and the energy change per atom converged to less than 5×10^{-7} eV atom^{-1}, yielding optimized structures using the virtual crystal approximation (Bellaiche & Vanderbilt, 2000; Sen & Ghosh, 2016). Electronic energy-loss spectra are calculated using experimental crystal structure (Katayama *et al.*, 2013) for monoclinic phase and space group symmetry $P2_1$. We use on-the-fly generated ultrasoft pseudo-potentials (Segall *et al.*, 2002), a plane-wave basis set with energy cutoff 500 eV, Brillouin zone (BZ) sampling in the k-space within the Monkhorst–Pack scheme (Monkhorst & Pack, 1976; Pack & Monkhorst, 1977) and grid size for self-consistent field calculation $13 \times 13 \times 10$. Here we perform our calculations using a $2 \times 2 \times 1$ supercell; these are large enough that the core-holes in neighbouring cells do not interact with each other.

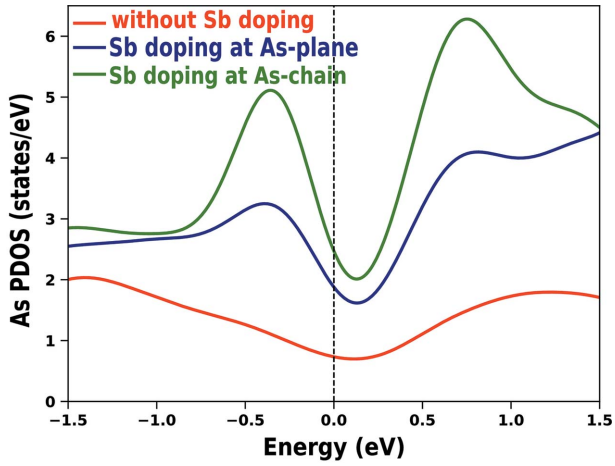

Figure 1
Partial density of states of As without Sb doping (in red), Sb doping at As sites belonging to the Fe–As plane (in blue), Sb doping at the As-chain (in green), of $Ca_{0.85}La_{0.15}Fe(As_{0.9}Sb_{0.1})_2$. The Fermi energy level is indicated by the vertical dashed line.

3. Result and discussion

In Fig. 1 we have presented atom and angular momentum projected PDOS of As in the case of three different samples: (i) $Ca_{0.85}La_{0.15}FeAs_2$, and a further 10% Sb doping at two different As sites, at the (ii) As-chain and (iii) Fe–As plane. The PDOS of As atoms belonging to the As-chain presented by the solid green line is significantly larger than that of Sb doping at the Fe–As plane presented in blue. The larger the DOS at the Fermi level, the larger will be the available electronic states for pairing in the superconducting states. This may be the reason for the larger observed T_c when Sb is doped in the chain As atom. This result indicates that the As zigzag chain structure, which is a unique characteristics of 112 IBSCs, may play a crucial role in increasing the critical temperature of 112 materials. Therefore, identification of the doping As site, whether in chain or plane, is essential. Below we show that this may be experimentally achieved either through ELNES or XANES study.

Theoretically computed As K-edge absorption spectra for IBSC material $Ca_{0.85}La_{0.15}FeAs_2$ are presented in Fig. 2, with [Fig. 2(ii)] and without [Fig. 2(i)] the core-hole effect being considered. In the case of As-plane K-edge absorption spectra, there are five distinct features indicated by A, B, C, D and E whereas the As-chain absorption spectra have four features A, B, F and G. The two spectra are distinctly different; this includes the 'pre-edge' region around A, the 'edge' region below B, as well as the ELNES/XANES region which is defined as higher in energy than B. Feature A is also reported in the case of other IBSCs (Cheng *et al.*, 2010, 2012). The difference in the 'pre-edge' for chain/plane As atoms reflects the difference in mixing of Fe and As states. The ionization edge for the As atom from the chain (blue dashed) and plane (solid red) occurs at different absorption energies. This observation is directly related to the oxidation state of As atoms, −3 for plane atoms and −1 for chain As atoms. Therefore in experimental XANES/ELNES studies a single

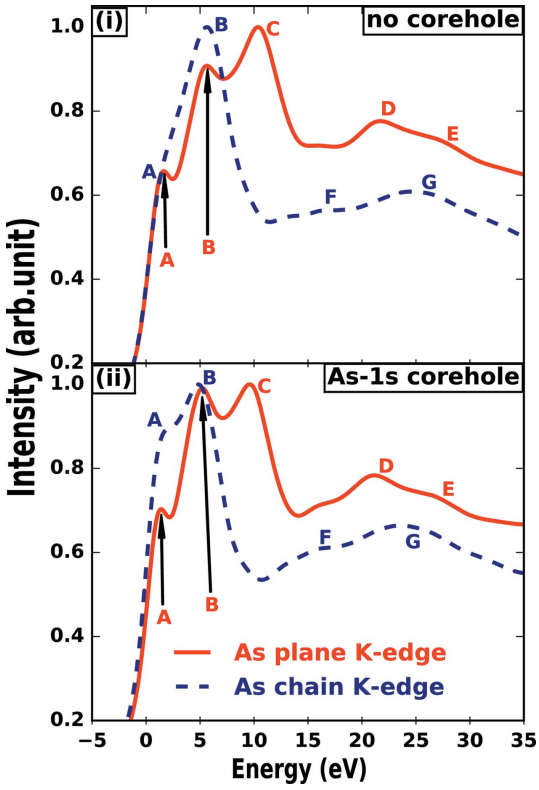

Figure 2
Comparison of As *K*-edge plane (red) and chain (blue) absorption spectra for $Ca_{0.85}La_{0.15}FeAs_2$. Comparison of spectra for (i) without and (ii) with As 1*s* core-hole. Special features are indicated by letters A–G.

As *K*-edge, corresponding to an oxidation state in between −1 and −3, is expected. The difference in the ELNES/XANES region reflects different atomic environments of the As chain and plane atoms. Lower- and higher-energy absorption regions are dominated by As chain and plane spectra, respectively.

The ionization edge for As (in the plane) occurs at higher energy compared with that of As-chain, indicating that the binding energies of As atoms at Fe_2–As_2 layers are greater than that of As atoms in the zigzag chain. Inclusion of the core-hole in the 1*s* state of the As atom from the plane caused pronounced features A and B with respect to that of no core-hole spectra. Features C and D are slightly blue-shifted in the presence of the core-hole. Feature E at a relatively higher energy does not exhibit core-hole effects. In the case of the chain As atom, feature A enhances significantly due to inclusion of the core-hole. Feature B is also slightly blue-shifted. Features F and G becomes pronounced and wider with inclusion of the core-hole. When a core-state electron is removed (a 'core-hole' being created), the electrostatic attraction on the remaining electrons from the nucleus is higher. This redistributes the electronic states closer to the Fermi level. Similarly, this greater electrostatic force contracts electronic states pulling closer together, thus increasing the intensity of the edge close to the Fermi level. Comparison of absorption spectra in the presence and absence of the core-hole effect is extremely important in our case. It is to be noted that the 112 materials are metals; there are a number of important works on metals that show that the ground-state calculations are in better agreement with experiment (Muller, 2009; Rez, 2006; Rez & Muller, 2008; Ross *et al.*, 2010). If the core-hole relaxes extremely fast, and so too the ensuing modification in the local DOS, in such a short time scale (compared with the time scale of transition of core-electron to conduction state) the changes will not be observable experimentally. While it is believed that Fe-based materials are correlated metals, relatively diffuse electrons will mean the core-hole is well screened, lessening its impact; experimentally determined spectra will determine whether core-holes are screened or not. In the case of the core-hole effect being substantial, the experimental edge is expected to be in between the dashed blue and solid red lines of Fig. 2(ii); depending on core-hole life time, experimental broadening *etc*., the two features B and C in Fig. 2(ii) may be broadened to a single feature. We thus believe that our result will play a significant role in experimentally identifying As-doping sites in 112 materials.

The origins of these special features are further explained in terms of site and angular momentum projected density of states. In Figs. 3 and 4 such efforts are presented in which the origins of various absorption peaks due to the type of dipole transition are self-explanatory. Vertical lines are used to locate the peak position of a particular peak of ELNES (top row) as well as that in the PDOS. Fig. 3(i) shows five distinct features A, B, C, D and E of *K*-edge absorption spectra including a core-hole in the As 1*s* state. The ground-state electronic configuration of the As atom is $[Ar]4s^23d^{10}4p^3$ and a dipole-allowed transition can occur from the core 1*s* state to any of the empty *p* states of As, as well as that of Ca, La and Fe. Feature A can be well described by transition to the As *p* state [see Fig. 3(ii)]; but the transition is weakened as As *p* states have a reasonable overlap with the *d* states of Fe and La [see Fig. 3(v)–3(vi)]. Feature B is well described by transition to the *p* states of both chain and plane As as well as that from La and Fe. A sizable amount of mixing with *d* states of Fe and La, Ca prohibits this absorption to be most intense compared with the C peak. Feature C has the highest peak height, described dominantly by transition to the *p* states of Ca–La and Fe [see the insets in Figs. 3(v)–3(vi)]. Features D and E occur in the relatively higher energy regions and are results of transitions to the *p* states of La (Ca) and Fe. They are weakened due to possible mixing of *d* and *p* states of Fe/Ca/La [see the inset window Fig. 3(v)]. Since the As-chains do not contain any Fe and have weaker bonding with La/Ca, the most intense peak C, as well as D and E, are completely absent in the chain As-*K* absorption spectra (see Fig. 4). The origin of the F and G features in Fig. 4 is also a result of transitions to the *p* states of La (Ca) and Fe, strongly damped by mixed *d* and *p* states of Fe/Ca/La [see window Fig. 4(v)]. This is essentially the origin of the differences in the As-*K* absorption spectra. Comparing our theoretical spectra with possible experimental measurements, the zero energy in Figs. 2, 3(i) and 4(i) should be taken as the experimental As-*K* edge = 11871 eV [see equation (2)] and the spectra should be a linear superposition of the same from both As chain and plane atoms.

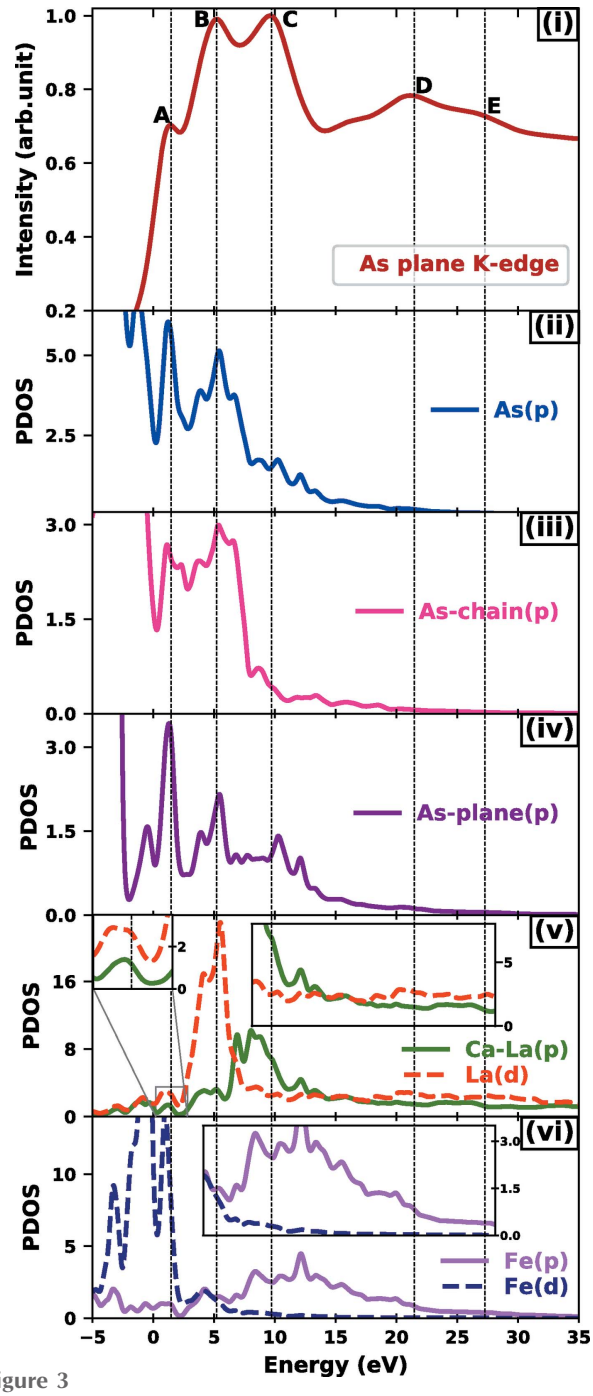

Figure 3
As K-edge absorption spectra of $Ca_{0.85}La_{0.15}FeAs_2$ and site projected density of states. (i) As plane K-edge absorption spectra including core-hole effect. (ii)–(vi): PDOSs of, from top to bottom, As p-DOS, As-chain p-DOS, As-plane p-DOS, Ca–La p-DOS and d-DOS, Fe p-DOS and d-DOS. Special features A, B, C, D and E are indicated by vertical dotted lines.

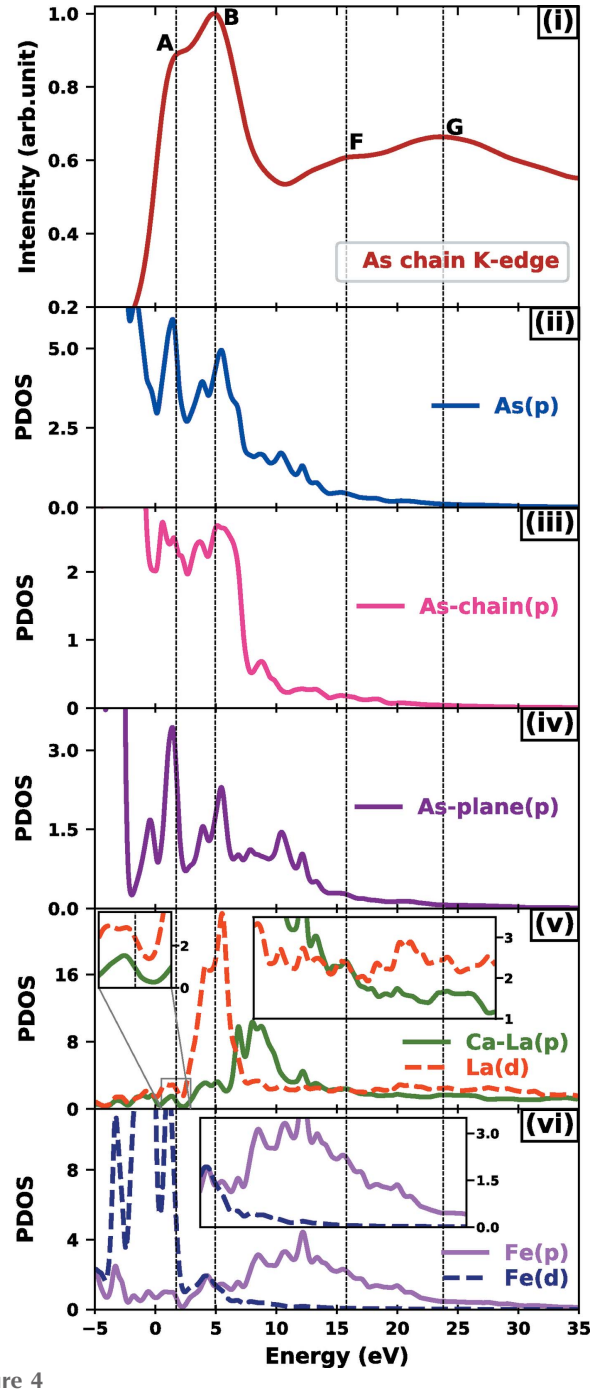

Figure 4
As K-edge absorption spectra of $Ca_{0.85}La_{0.15}FeAs_2$ and site projected density of states. (i) As chain K-edge absorption spectra including core-hole effect. (ii)–(vi): PDOSs of, from top to bottom, As p-DOS, As-chain p-DOS, As-plane p-DOS, Ca-La p-DOS and d-DOS, Fe p-DOS and d-DOS respectively. Special features A, B, F and G are indicated by vertical dotted lines.

In the absence of any available experimental XANES data on 112 IBSCs it would be instructive to apply the theoretical methodology presented in this work to the other IBSC materials on which experimental as well as other theoretical calculations are already available. One such work, on $FeTe_{1-x}Se_x$, was published by Mulato-Gómez *et al.* (2014). In Fig. 5(*a*) we present Fe K-edge absorption spectra of FeSe, using DFT-based theoretical calculation as described above in the presence and absence of a 'core-hole'. Excellent agreement between the absorption spectra in Fig. 5(*a*) with that of experimental data [Fig. 1(*a*) of Mulato-Gómez *et al.* (2014)] is worth noting. The experimental data were earlier compared with calculation using a different theoretical approach to ours, *i.e.* real-space multiple-scattering formalism using clusters of

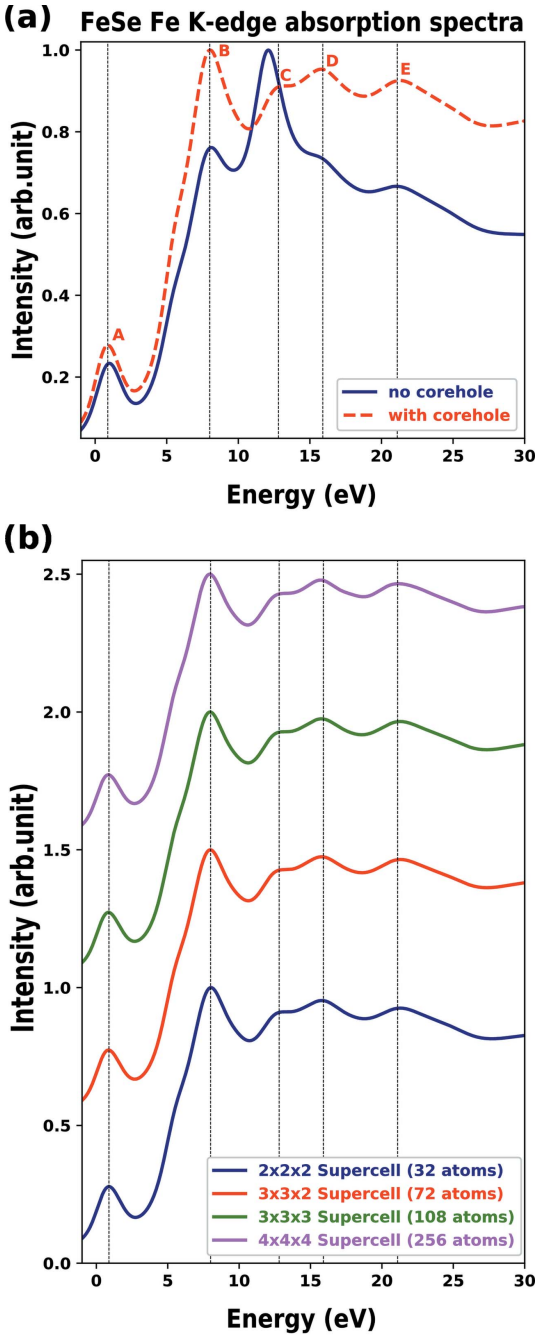

Figure 5
Fe *K*-edge absorption spectra of FeSe (*a*), with core-hole effect (red curve) and without core-hole effect (blue curve). (*b*) FeSe Fe *K*-edge absorption spectra with variable supercell size, vertically shifted by 0.5 units for clarity.

radius 6 Å (Mulato-Gómez *et al.*, 2014). It is worth mentioning that both the theoretical methods reproduce the experimental data; while our method uses periodic bulk systems, the multiple-scattering calculation considers finite clusters. In Fig. 5(*b*) the supercell size independence of the absorption spectra ensures that there is no effect of 'core-hole–core-hole interaction. We have also extended a comparison of our method for other IBSC materials for which experimental data are available (Cheng *et al.*, 2010, 2012; Joseph *et al.*, 2010).

4. Conclusions

We have presented density functional theory based core-electron spectroscopic studies on iron-based superconducting 112 material. We emphasize the importance of identifying As-doping cites. Sb doping at the chain As-site enhances respective partial DOS which may be related to enhancing superconducting T_c. Theoretically computed As *K*-edge absorption spectra for $Ca_{0.85}La_{0.15}FeAs_2$ for two different kinds of As atoms, from the plane as well as from the chain, show remarkably different absorption edges as well as the spectra in general. The As (chain/plane) *K*-edge absorption spectra in the presence and absence of the 'core-hole effect' are presented for future possible identification of the same experimentally. In both cases the absorption spectra contain several features, the origin of which are thoroughly described using site projected density of states results. The theoretical methods used in this work are also shown to agree with observed core-electron spectroscopic data for other IBSC materials as well as multiple-scattering methods. We believe this work will attract further research in this field.

Acknowledgements

We thank Dr P. A. Naik, Dr A. K. Sinha for support and discussions. Support of RRCAT scientific computer centre is acknowledged. SG also acknowledges the HBNI, RRCAT for financial support and encouragements.

References

Bellaiche, L. & Vanderbilt, D. (2000). *Phys. Rev. B*, **61**, 7877–7882.
Bianconi, A., Menushenkov, A. P., Ivanov, V. G., Ivanov, A. A. & Joseph, B. (2017). *J. Phys. Conf. Ser.* **941**, 012058.
Blöchl, P. E. (1994). *Phys. Rev. B*, **50**, 17953–17979.
Broyden, C. G. (1970). *J. Appl. Math.* **6**, 76.
Caglieris, F., Sala, A., Fujioka, M., Humme, F., Pallecchi, I., Lamura, G., Johrendt, D., Takano, Y., Ishida, S., Iyo, A., Eisaki, H., Ogino, H., Yakita, H., Shimoyama, J. & Putti, M. (2016). *APL Mater.* **4**, 020702.
Cheng, J., Chu, W. S., Wu, G., Zhao, H. F., Xu, W., Zhou, J., Zhang, L. J., Chen, X. H. & Wu, Z. Y. (2010). *J. Synchrotron Rad.* **17**, 730–736.
Cheng, J., Zhou, J., Hu, R., Xu, W., Li, Y., Zhang, L., Marcelli, A., Chu, W., Xu, Z. & Wu, Z. (2012). *New J. Phys.* **14**, 033005.
Clark, S. J., Segall, M. D., Pickard, C. J., Hasnip, P. J., Probert, M. J., Refson, K. & Payne, M. C. (2005). *Z. Kristallogr.* **200**, 567.
Egerton, R. F. (1996). *Electron Energy-Loss Spectroscopy in the Electron Microscope*, 2nd ed. New York: Plenum Press.
Fletcher, R. (1970). *Comput. J.* **13**, 317–322.
Gao, S. P., Pickard, C. J., Payne, M. C., Zhu, J. & Yuan, J. (2008). *Phys. Rev. B*, **77**, 115122.
Gao, S. P., Pickard, C. J., Perlov, A. & Milman, V. (2009). *J. Phys. Condens. Matter*, **21**, 104203.
Gao, S. P., Zhang, A., Zhu, J. & Yuan, J. (2004). *Appl. Phys. Lett.* **84**, 2784–2786.
Ghosh, A. & Ghosh, H. (2019). *Comput. Mater. Sci.* **160**, 62–71.
Ghosh, A., Ghosh, H. & Sen, S. (2019). *Intermetallics*, **107**, 126–136.
Goldfarb, D. (1970). *Math. C.* **24**, 23.
Guo, Q., Ding, J., Tanaka, T., Nishio, M. & Ogawa, H. (2005). *Appl. Phys. Lett.* **86**, 111911.
Huang, Y.-N., Yu, X.-L., Liu, D.-Y. & Zou, L.-J. (2015). *J. Appl. Phys.* **117**, 17E113.

Ivanov, A. A., Ivanov, V. G., Menushenkov, A. P., Wilhelm, F., Rogalev, A., Puri, A., Joseph, B., Xu, W., Marcelli, A. & Bianconi, A. (2018). *J. Supercond. Nov. Magn.* **31**, 663–670.
Jayawardane, D. N., Pickard, C. J., Brown, L. M. & Payne, M. C. (2001). *Phys. Rev. B*, **64**, 115107.
Joseph, B., Iadecola, A., Simonelli, L., Mizuguchi, Y., Takano, Y., Mizokawa, T. & Saini, N. L. (2010). *J. Phys. Condens. Matter*, **22**, 485702.
Kamihara, Y., Watanabe, T., Hirano, M. & Hosono, H. (2008). *J. Am. Chem. Soc.* **130**, 3296–3297.
Katayama, N., Kudo, K., Onari, S., Mizukami, T., Sugawara, K., Sugiyama, Y., Kitahama, Y., *Iba*, K., Fujimura, K., Nishimoto, N., Nohara, M. & Sawa, H. (2013). *J. Phys. Soc. Jpn*, **82**, 123702.
Kosog, B., La Pierre, H. S., Denecke, M. A., Heinemann, F. W. & Meyer, K. (2012). *Inorg. Chem.* **51**, 7940–7944.
Kudo, K., Kitahama, Y., Fujimura, K., Mizukami, T., Ota, H. & Nohara, M. (2014). *J. Phys. Soc. Jpn*, **83**, 093705.
Kudo, K., Mitsuoka, D., Takasuga, M., Sugiyama, Y., Sugawara, K., Katayama, N., Sawa, H., Kubo, H. S., Takamori, K., Ichioka, M., Fujii, T., Mizokawa, T. & Nohara, M. (2013). *Sci. Rep.* **3**, 3101.
Liu, Z.-H., Kim, T. K., Sala, A., Ogino, H., Shimoyama, J., Büchner, B. & Borisenko, S. V. (2015). *Appl. Phys. Lett.* **106**, 052602.
Liu, Z. T., Xing, X. Z., Li, M. Y., Zhou, W., Sun, Y., Fan, C. C., Yang, H. F., Liu, J. S., Yao, Q., Li, W., Shi, Z. X., Shen, D. W. & Wang, Z. (2016). *Appl. Phys. Lett.* **109**, 042602.
Mizuguchi, Y., Paris, E., Wakita, T., Jinno, G., Puri, A., Terashima, K., Joseph, B., Miura, O., Yokoya, T. & Saini, N. L. (2017). *Phys. Rev. B*, **95**, 064515.
Monkhorst, H. & Pack, J. D. (1976). *Phys. Rev. B*, **13**, 5188–5192.
Mulato-Gómez, D. F., Mustre de León, J. & Saini, N. L. (2014). *J. Supercond. Nov. Magn.* **27**, 1035–1040.
Muller, D. A. (2009). *Nat. Mater.* **8**, 263–270.
Nagai, Y., Nakamura, H., Machida, M. & Kuroki, K. (2015). *J. Phys. Soc. Jpn*, **84**, 093702.
Ota, H., Kudo, K., Kimura, T., Kitahama, Y., Mizukami, T., Ioka, S. & Nohara, M. (2017). *J. Phys. Soc. Jpn*, **86**, 025002.
Pack, J. & Monkhorst, H. J. (1977). *Phys. Rev. B*, **16**, 1748–1749.
Paris, E., Simonelli, L., Wakita, T., Marini, C., Lee, J. -H., Olszewski, W., Terashima, K., Kakuto, T., Nishimoto, N., Kimura, T., Kudo, K., Kambe, T., Nohara, M., Yokoya, T. & Saini, N. L. (2016). *Sci. Rep.* **6**, 27646.
Perdew, J. P., Burke, K. & Ernzerhof, M. (1996). *Phys. Rev. Lett.* **77**, 3865–3868.
Pickard, C. J. & Payne, M. C. (1997). *Electron. Microsc. Anal.* **153**, 179.
Pickard, C. J., Payne, M. C., Brown, L. M. & Gibbs, M. N. (1995). *Electron. Microsc. Anal.* **147**, 211.
Rez, P. (2006). *Microsc. Microanal.* **12**(Suppl.2), 108.
Rez, P. & Muller, D. A. (2008). *Annu. Rev. Mater. Res.* **38**, 535–558.
Ross, I. M., Rainforth, W. M., Seabourne, C. R., Scott, A. J., Wang, P., Mendis, B. G., Bleloch, A. L., Reinhard, C. & Hovsepian, P. E. (2010). *Thin Solid Films*, **518**, 5121–5127.
Sarangi, R. (2018). *J. Synchrotron Rad.* **25**, 944–952.
Segall, M. D., Lindan, P. J. D., Probert, M. J., Pickard, C. J., Hasnip, P. J., Clark, S. J. & Payne, M. C. (2002). *J. Phys. Condens. Matter*, **14**, 2717–2744.
Sen, S. & Ghosh, H. (2016). *Eur. Phys. J. B*, **89**, 277.
Shanno, D. F. (1970). *Math. C.* **24**, 647.
Singh, H., Topsakal, M., Attenkofer, K., Wolf, T., Leskes, M., Duan, Y., Wang, F., Vinson, J., Lu, D. & Frenkel, A. I. (2018). *Phys. Rev. Mater.* **2**, 125403.
Sinha, M., Modi, M. H., Ghosh, H., Yadav, P. K. & Gupta, R. K. (2018). *J. Synchrotron Rad.* **25**, 771–776.
Wu, X., Le, C., Liang, Y., Qin, S., Fan, H. & Hu, J. (2014). *Phys. Rev. B*, **89**, 205102.
Xie, T., Gong, D., Ghosh, H., Ghosh, A., Soda, M., Masuda, T., Itoh, S., Bourdarot, F., Regnault, L. P., Danilkin, S., Li, S. & Luo, H. (2018). *Phys. Rev. Lett.* **120**, 137001.